

Airfoil trailing-edge noise source identification using large-eddy simulation and wavelet transform

By S. Lee[†], D. Kang[†], D. Brouzet AND S. K. Lele

Airfoil noise is predicted and analyzed using wall-resolved large-eddy simulations and wavelet transforms for a NACA 0012 airfoil at a Mach number of 0.06 and a Reynolds number of 400,000 using a stair-strip forced transition and a natural transition. At a high angle of attack, vortex shedding and a laminar separation bubble (LSB) occur on the suction side. The LSB triggers the flow transition for both the forced and natural transition cases. The wavelet thresholding and denoising algorithm is used to decompose the pressure fields into the coherent or denoised pressure and the incoherent or background noise pressure. This denoising technique provides a clear picture of true noise generation and propagation. It also reveals the dominant noise source at specific frequencies when multiple noise sources are present. In another usage, the wavelet thresholding algorithm with down-sampling separates noise on the basis of flow structures. For example, the wavelet method separates noise between low-frequency vortex shedding noise and high-frequency LSB noise as well as trailing-edge noise. Finally, the wavelet transform is used to decompose the hydrodynamic and acoustic pressure components near the surface using the coherence between near-field pressure and far-field pressure. Overall, the wavelet-based decomposition is a valuable tool to study and reveal the mechanisms of airfoil noise generation.

1. Introduction

Turbulent boundary layer trailing-edge noise is an important fluid mechanics problem involving a turbulent flow and its interaction with a solid body (Lee et al. 2021). This noise is generated when turbulent boundary layer pressure fluctuations are scattered by a sharp edge or they experience a sudden change in the boundary conditions. This problem occurs for many aerospace and industrial applications, such as aircraft wings, rotorcrafts, wind turbines, or propellers. In particular, the recent advent of electric vertical takeoff and landing or urban air mobility aircraft further increased interest in this trailing-edge noise because this noise becomes more apparent at low RPM with more blades (Greenwood et al. 2022; Li & Lee 2020, 2021, 2022).

Large-eddy simulations (LES) have been applied to predict trailing-edge noise at low Reynolds numbers (Wolf & Lele 2012; Bodling & Sharma 2019). The accuracy of numerical simulations depends on many parameters, including the grid resolution, time step, and numerical scheme. For example, if the grid resolution is not sufficient, unphysical numerical noise or background noise occurs at high frequencies (Brouzet 2020). It is important to identify and eliminate this numerical noise in the time-domain pressure fields and frequency-domain spectra to capture only true or physical noise sources.

Although trailing-edge noise is an important component of airfoil broadband noise, especially at high frequencies, there are also other competing noise sources, such as

[†] Department of Mechanical and Aerospace Engineering, University of California, Davis

vortex shedding noise, laminar separation bubble (LSB) instability noise, tip noise, stall noise, and tripping noise (Brooks et al. 1989). In particular, vortex shedding noise is observed as tonal noise at low frequencies. LSB and tripping noise that exhibit tonal and broadband noise characteristics at high frequencies are affected by flow conditions, airfoil geometries, angles of attack, numerical tripping methods, and so on. It is desirable to separate the acoustic fluctuations arising from physically different noise sources.

Based on the acoustic analogy, the pressure fluctuation on the surface is the dipole noise source (Amiet 1976). The unsteady and random pressure fluctuations associated with trailing-edge noise include two major components: hydrodynamic turbulent pressure fluctuations and acoustic pressure fluctuations due to the scattering by a trailing edge. In incompressible flow simulations, the acoustic scattering is not captured, so it should be separately accounted for. The hydrodynamic wall pressure fluctuations can be independently determined as well (Lee 2018; Lee & Shum 2019). For compressible flow simulations, both the hydrodynamic and acoustic parts are captured. However, it is difficult to distinguish these two components and analyze their relative contributions to far-field acoustics. As new noise reduction techniques, such as serrations or finlets, are being developed, distinguishing these source components becomes important, as this distinction reveals an exact source of noise generation and provides means to control such noise.

Wavelet transform methods have proved useful to decompose the pressure fields in turbulent flows (Farge 1992; Schneider & Vasilyev 2010) and, more recently, in jet aeroacoustics (Mancinelli et al. 2017). In the wavelet thresholding technique, the magnitudes of wavelet coefficients are divided into two categories based on the selection of an appropriate threshold. These categories were identified as coherent and incoherent fields (Schneider & Vasilyev 2010). For example, the wavelet thresholding denoising technique was used to filter out nearly Gaussian white noise, which was identified as the incoherent field, and to retain only the coherent vortical fields (Azzalini et al. 2005; Nguyen van yen et al. 2012).

In our research, we use the wavelet-based decomposition method to address various important questions in airfoil noise. The first goal is to identify and eliminate numerical noise and provide the denoised pressure fields. This will help reveal true noise sources in numerical simulations. The second goal is to separate the acoustic pressure fields depending on the flow structures or noise sources. Finally, we separate the hydrodynamic pressure from the acoustic pressure in airfoil noise using the wavelet transform and the coherence between the near-field pressure and far-field pressure.

2. Methodology

2.1. LES computational setup

The numerical method was developed and described by Kang & Lee (2022). For completeness, the method is briefly described in this section.

The computational domain and a NACA 0012 airfoil with a blunt trailing-edge configuration adopted in the present study are presented in Figure 1(a,b). Two angles of attack, 0° and 6.25° , are considered. The airfoil chord length is denoted by c . A two-dimensional O-grid has a radius of $8.0c$ and is extruded in the spanwise direction whose length is $0.1c$. The no-slip boundary is applied on the airfoil surface. For the far field, the freestream boundary condition is imposed in which the Riemann invariant is used depending on the flow direction at the boundary, and the nonreflecting boundary condition is also applied

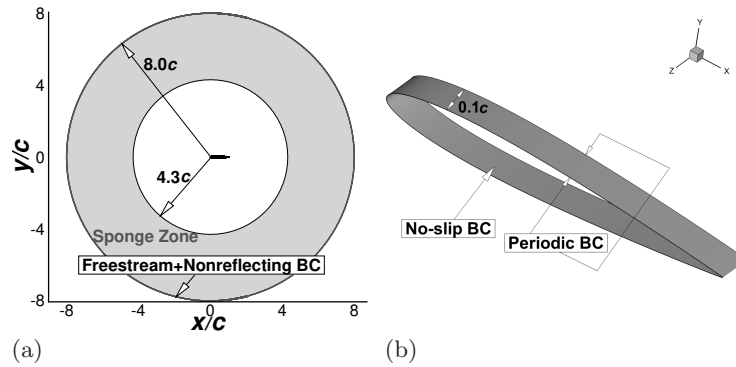


FIGURE 1. CFD domain: (a) O-type computational domain over the far field and (b) the three-dimensional airfoil surface with boundary conditions (BCs).

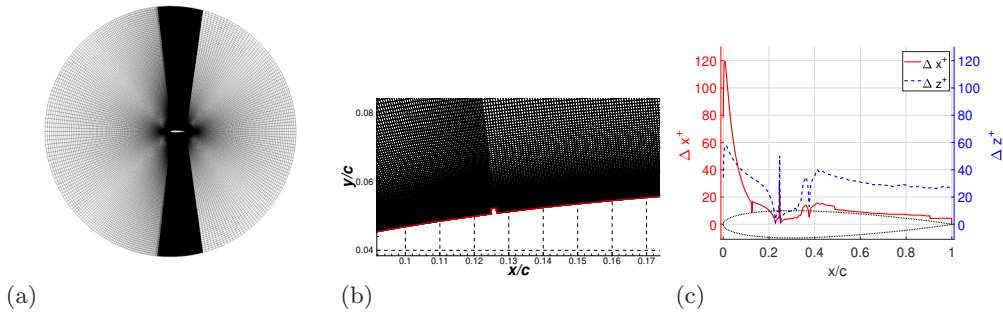


FIGURE 2. CFD mesh: (a) structured mesh over the whole domain as a plane view, (b) enlarged near-wall view around the stair-shaped tripdot, and (c) grid spacing in wall units along the suction side of the airfoil.

in order to prevent sound waves from being reflected from the far-field domain back to the source of sound. The periodic condition is applied in the spanwise direction for a three-dimensional simulation. Finally, a sponge zone is placed between the radius of $4.3c$ and the far field to dissipate sound energy and minimize reflections. Wave strength is gradually reduced in the sponge zone. The damping coefficient in the artificial damping term introduced in the Navier-Stokes equations is defined as ν_{max} whose optimized value is prescribed as 2 MHz.

Using Gmsh (Geuzaine et al. 2009), the structured mesh is generated to span from the NACA 0012 to the O-grid whole domain, as shown in Figure 2(a,b). The size of the cell distribution is $N_x \times N_y \times N_z = 4308 \times 323 \times 65$ in the streamwise, normal, and spanwise directions, respectively, including both the near-wall and background fields. The grid distribution on the suction and pressure sides is symmetric; thus, the total number of grid points is 90,442,300. Two transition cases are considered: stair-strip enforced transition and natural transition. For the forced transition, the tripdot is placed at $x/c = 0.125$ on both the suction and pressure sides to trigger the transition to turbulent flows. One can see the stair-shaped tripdot installed on the suction side in Figure 2(b). The non-dimensional stair-strip height is 60 viscous wall unit length, which is between smooth and fully rough cases. The grid is designed to resolve the near-wall flow fields and thus capture acoustic sources. Approximately 120 grid points are generated within the boundary layer

near the trailing edge. Figure 2(c) shows that Δx^+ is less than 20 and Δz^+ less than 40 downstream of the tripdot point. Note that the grid spacing in the wall units is drawn along the suction side only. Furthermore, y^+ is maintained at less than 0.1 along the entire airfoil surface in the present simulation. As shown by Kang & Lee (2022), the present grid resolution is satisfactory for wall-resolved LES (Lee et al. 2021).

Compressible LES is conducted for the flow past NACA 0012 with a blunt trailing edge. Finite-volume-based rhoPimpleFoam built in OpenFOAM (v2012) (Weller et al. 1998) is employed to simulate unsteady compressible flows. The spatial discretization is performed using the Gauss linear scheme, and the temporal discretization uses the backward-differencing scheme, both of which are second-order accurate. The time step is set to be 10^{-6} s, corresponding to a maximum Courant-Friedrichs-Lewy number of 0.9. The inner loop per one physical time step is iterated until the convergence criterion is satisfied, which is 10^{-10} in this study. Eddies greater than the grid size are fully resolved, whereas eddies smaller than the grid size are modeled by incorporating wall-adapting local eddy viscosity in the governing equation as a closure model. The initial condition for LES is obtained from the steady-state Reynolds-averaged Navier-Stokes simulation for which k - ω shear stress transport is adopted as a closure model. The steady-state flow solver used is rhoSimpleFoam. The total simulation time in LES corresponds to 20 airfoil flow-through times (FTT). The data for spectral processing and acoustic computation are collected from the last 10 FTT in which flows reach a statistically convergent state. The parallel computations are made over computational domains decomposed through OpenMPI, and the elapsed calculation time was roughly 148,043 s per FTT using 256 cores on CPU 3.3 GHz, which corresponds to 210,550 total CPU-hours, at the UC Davis High-Performance Computing Core Facility.

2.2. Wavelet-based decomposition

The continuous wavelet transform of a random pressure fluctuation in the time domain $p(t)$ consists of a projection over a basis of compact support functions obtained by dilation and translation of the mother wavelet $\Psi(t)$, which is localized in both the time and frequency domains. The resulting wavelet coefficient is a function of time t and of the scale s , the latter being inversely proportional to frequency. The continuous wavelet coefficient is defined as:

$$w(s, t) = C_{\Psi}^{-1/2} s^{-1/2} \int_{-\infty}^{\infty} \Psi^* \left(\frac{\tau - t}{s} \right) p(\tau) d\tau, \quad (2.1)$$

where $\Psi^*((t - \tau)/s)$ is the complex conjugate of the dilated and translated $\Psi(t)$ and $C_{\Psi}^{-1/2}$ is obtained satisfying the admissibility condition

$$C_{\Psi} = \int_{-\infty}^{\infty} |\omega|^{-1} |\hat{\Psi}(\omega)|^2 d\omega < \infty. \quad (2.2)$$

Here $\hat{\Psi}(\omega)$ is the Fourier transform of $\Psi(t)$,

$$\hat{\Psi}(\omega) = \int_{-\infty}^{\infty} \Psi(t) e^{-j\omega t} dt. \quad (2.3)$$

For a discretized domain as in the present study, a discrete wavelet transform (DWT) is utilized in practice. A stationary time series of pressure fluctuation is decomposed by

DWT. The discrete wavelet coefficients are given by

$$w_p^{(s)}(n) = \sum_{k=-\infty}^{+\infty} \Psi^s(n - 2^s k) p(k), \quad (2.4)$$

where s denotes the discretized scale, while the wavelet function $\Psi^s(n - 2^s k)$ is the discretized version of $\Psi^s = 2^{-s/2} \Psi(t/2^s)$. The wavelet kernel used is the Daubechies-12 type. The wavelet coefficients obtained from DWT are used in a separation algorithm to isolate the coherent part of the pressure from the incoherent part of the pressure. A nonlinear recursive denoising technique is used in the present work (Azzalini et al. 2005). The incoherent source of the pressure is iteratively filtered until the convergence criterion is satisfied. Originally, based on statistical reasoning (Donoho & Johnstone 1994), a threshold was guessed as

$$T_o = \sqrt{2 \langle p'^2 \rangle \log_2 N_s}, \quad (2.5)$$

where $\langle p'^2 \rangle$ is the variance of the pressure signal and N_s is the number of samples. Starting from the initial guess above, the threshold is updated at each iteration in the loop whose formulation can be written as

$$T_i = \sqrt{2 \langle p_i'^2 \rangle \log_2 N_s}, \quad (2.6)$$

where $\langle p_i'^2 \rangle$ indicates the variance of the incoherent part of the pressure signal in time at the i th iteration. The threshold is converged within 20 iterations in the present work. Such wavelet analysis has been carried out in MATLAB.

3. Results

3.1. Flow and acoustic results

The validations of the mean flow and wall pressure spectra at a zero angle of attack were presented by Kang & Lee (2022). For the sake of brevity, the validations are not presented in this paper. At a 6.25° angle of attack, the LSB upstream of the stair strip on the suction side and vortex shedding near the trailing edge on the pressure side are observed, as shown in Figure 3(a,b).

Figure 4 shows the sound pressure level for stair-strip tripping and natural transition cases at a high angle of attack. The observer location is $(x/c, y/c, z/c) = (1.0, 0.05, 4.07)$ with a chord length, c , of 0.3 m. The coordinates x, y , and z denote the streamwise, spanwise, and wall-normal directions, respectively. Tonal noise appears at around 560 Hz due to the vortex shedding and at around 3 kHz due to LSB instability. Although it is not shown in this report, the root mean square of the pressure fluctuations exhibits a strong peak near the LSB region, which confirms the noise source location. Although the magnitude is low compared with the tonal noise, the trailing-edge broadband noise occurs beyond 2 kHz. The visualization of the noise propagation at specific frequencies will confirm all these noise sources with the aid of the wavelet-based decomposition method in the next subsection.

3.2. Wavelet-based decomposed pressures

First, the wavelet thresholding technique is used to identify the numerical noise. Figure 5(a,b) shows the decomposed wall pressure spectrum at $x/c = 0.99$ and the sound

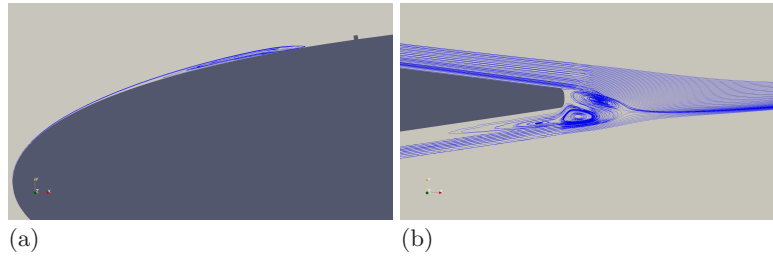


FIGURE 3. Streamlines for (a) a laminar separation bubble on the suction side upstream of the stair strip and (b) vortex shedding on the pressure side near the trailing edge.

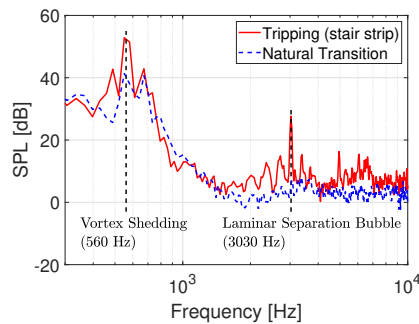


FIGURE 4. Sound pressure level (SPL) for tripping and natural transition cases at an angle of attack of 6.25° .

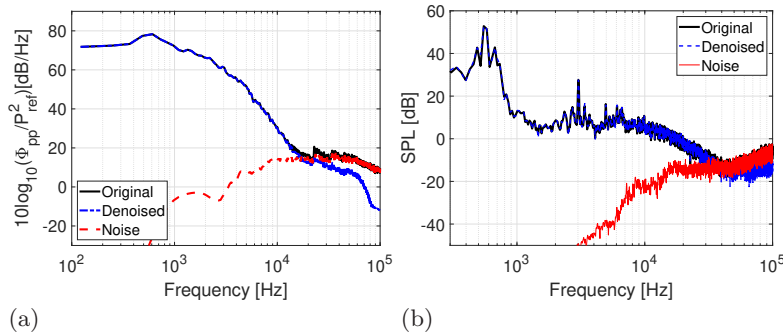


FIGURE 5. (a) Decomposed wall pressure spectrum at $x/c = 0.99$ and (b) decomposed power spectral density at $(x/c, y/c, z/c) = (1.0, 0.05, 4.07)$.

power spectral density at the same observer as that used in Figure 4. The Nyquist frequency or half of the sampling frequency is 500 kHz in both panels. A Hanning window was used to generate these spectra. The figure shows that the original wall pressure spectrum has a plateau beyond 20 kHz and is mostly spurious numerical noise. The magnitude of numerical noise is low at low frequencies or below 10 kHz, where the denoised or physical pressure is dominant. This indicates that the numerical noise is not perfectly white noise. In the SPL plot, the numerical noise contributes only beyond 40 kHz.

Figure 6(a-c) presents the dilatation fields of the original pressure as well as the denoised pressure and the numerical noise pressure at a zero angle of attack. The numerical noise is evident near the tripping region and the trailing-edge region. The numerical noise propagates with the speed of sound so that it can be misunderstood as the acoustic pres-

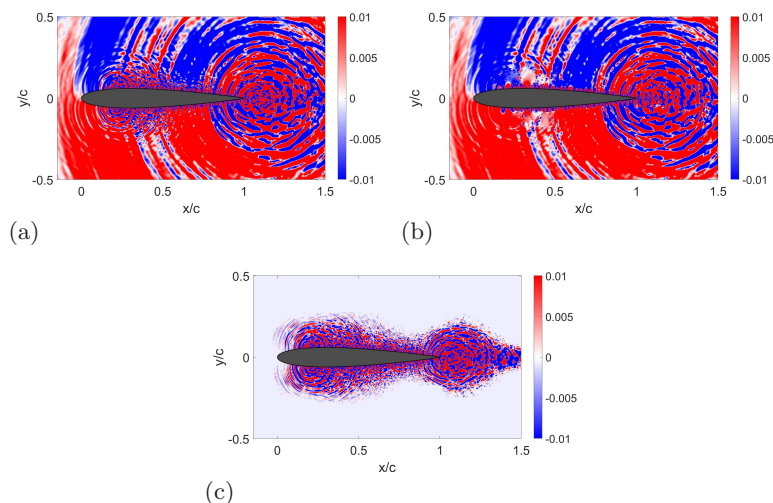


FIGURE 6. Dilatation fields cut at midspan for (a) the original pressure, (b) the denoised pressure, and (c) the noise pressure at a zero angle of attack.

sure (Kang & Lee 2022). After eliminating the numerical noise, the denoised pressure field shows a clearer picture of the convecting coherent turbulent structures as well as physical noise propagation. The figure shows that the noise originating from the tripping region is actually numerical noise so that the true dominant noise source is trailing-edge noise in this case. In sum, the wavelet-based decomposition method reveals true noise source generation and propagation without numerical noise contamination. Although not shown here, 6.25° angle of attack cases show that the numerical noise is not significant compared with the physical noise so that the original pressure and denoised pressure look similar. The LSB plays a role in generating significant physical noise, as shown in Figure 4, which is much stronger than the numerical noise.

Second, the original pressure is down-sampled with the Nyquist frequency of 10 kHz before the wavelet transform is applied. The same thresholding technique is used, where the pressure reconstructed with the wavelet coefficients whose magnitudes are larger than the threshold value is denoted P_1 and the remaining pressure is denoted P_2 . Figure 7(a,b) shows the contours of the cross-spectrum level, defined as $\text{SPSL}(\text{dB}) = 10 \log_{10}(|S_{xy}| \Delta f / p_{ref}^2)$, between a point near the trailing edge and points in the two-dimensional field for P_1 and P_2 at 500 Hz and 6 kHz, respectively, where S_{xy} is the two-point cross spectrum, $\Delta f = 1/T = 6.67$ Hz, and $p_{ref} = 20 \mu\text{Pa}$. Although not shown here, the cross-spectrum contours of P_1 become zero at high frequencies, while the cross-spectrum contours of P_2 become zero at low frequencies. This indicates that P_1 represents the low-frequency vortex shedding noise and P_2 represents the high-frequency noise that contains the LSB instability noise and trailing-edge noise. The leading-edge noise generated from the LSB instability is more evident than the trailing-edge noise in Figure 7(b), even though the reference point is located at the trailing edge when computing the cross-spectrum-level contour plots. This indicates that the pressure at the trailing edge is strongly influenced by the leading-edge noise or that the leading-edge noise is stronger than the trailing-edge noise in this case. In sum, the wavelet-based decomposition technique with down-sampling, that is, without any high-frequency numerical noise, is useful to separate the

noise sources as well as their acoustic propagation depending on flow structures or noise sources.

Finally, the wavelet transform is used to separate the hydrodynamic pressure from the acoustic pressure near the surface. The main idea is to use the cross-correlation or coherence between the pressure near the surface and far-field pressure. A key assumption is that the acoustic pressure near the wall is strongly correlated with the far-field pressure while the hydrodynamic pressure is less correlated with the far-field pressure. There is still a challenge in this approach. The magnitudes of specific wavelet coefficients from the pressure near the surface contain both the hydrodynamic and acoustic contributions so that separation cannot be achieved by just sorting out the wavelet coefficient magnitudes using the threshold denoising technique, which was used in jet noise (Mancinelli et al. 2017). In our new algorithm, the extent of the acoustic contribution in the wavelet coefficient magnitude is determined from the coherence between the pressure near the surface and far-field pressure. Figure 8(a) shows the flow chart of the algorithm. After performing DWT of the original near-wall pressure, the index, k , of the wavelet coefficient is determined on the basis of the low-pass filter (LPF) cutoff value, which is assumed to be 0.96 in the current study. This value was selected when the sum of the wavelet coefficients squared reaches plateau. Therefore, this cutoff value can be case dependent. The near-wall wavelet coefficients below this index or the point of LPF are retained. Above this range, the wavelet coefficients of the far-field acoustic pressure (ω_{FAR}) are taken due to the dominance of the hydrodynamic pressure in this range for the near-wall pressure. In the next step, the wavelet coefficients for the guessed near-wall acoustics ($\tilde{\omega}_{NW,ac,guess}$) are used to find the acoustic pressure through inverse DWT (IDWT). The coherence between the guessed near-wall acoustic pressure and the far-field pressure is used to determine the final near-wall acoustic pressure. Finally, the hydrodynamic pressure ($p_{NW,hy}$) is obtained by subtracting the acoustic pressure ($p_{NW,ac}$) from the total pressure. Figure 8(b) shows the original pressure, hydrodynamic pressure, and acoustic pressure near the trailing edge on the suction side using this algorithm. For the validation, the hydrodynamic and acoustic pressures are also obtained from the wavenumber-frequency-domain Fourier transform approach. Although the results are not perfectly matched, the new method shows the correct tonal peaks at 500 Hz, 3 kHz, and 5 kHz. The acoustic pressure also captures the right trend at high frequency, which exhibits a rapid decay. The hydrodynamic pressure in the new method follows the original pressure in almost the entire frequency range, while the wavenumber-frequency-domain Fourier transform result shows a higher hydrodynamic pressure than the original pressure at high frequency, which might be possible with the destructive interference between the hydrodynamic and acoustic pressures. In sum, the new method provides promising results for decomposing the hydrodynamic and acoustic pressures. Yet, more work is needed to improve the results.

4. Conclusions

This paper has applied the wavelet transform approach to airfoil aerodynamic noise to decompose the pressure in various useful ways. First, the wavelet-based thresholding denoising technique identifies and eliminates the nearly Gaussian numerical noise. The numerical noise is dominant near the tripping- and trailing-edge regions at high frequencies. Second, the same wavelet technique with down-sampling decomposes the acoustic pressure into low-frequency vortex shedding noise and high-frequency LSB instability

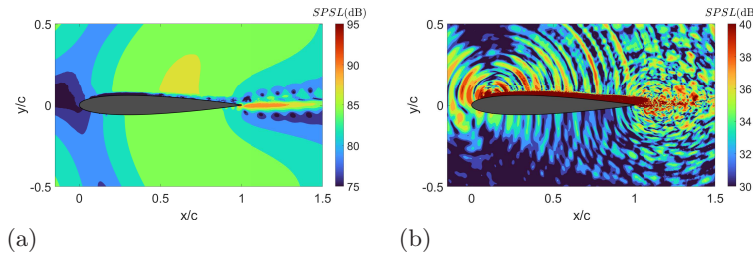


FIGURE 7. Contours of the cross-spectrum level using the wavelet-based decomposed pressures with down-sampling: (a) P_1 at 500 Hz and (b) P_2 at 6 kHz. The reference point for the cross spectrum is located at the trailing edge.

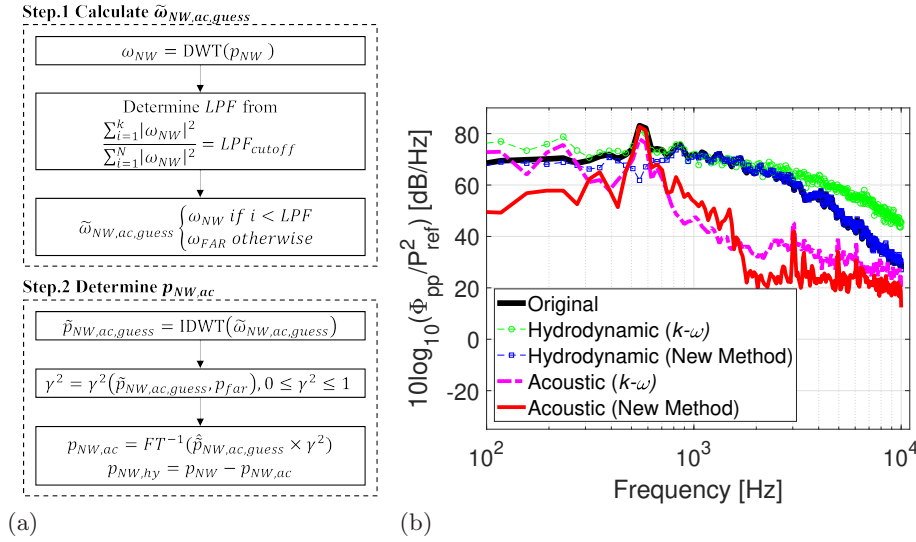


FIGURE 8. (a) Flow chart of the numerical algorithm for the new decomposition method and (b) the results of the decomposed pressures near the trailing edge.

noise as well as trailing-edge noise. Third, the coherence between near-field pressure and far-field pressure was applied to the wavelet coefficients to decompose the hydrodynamic and acoustic pressures in the near field. Yet, this method needs further improvement to achieve more precise separation between the two pressure components.

It is expected that this novel technique will provide new insights into airfoil noise generation and propagation mechanisms. For example, the separation between the hydrodynamic and acoustic pressures helps improve and guide the low-fidelity acoustic prediction model developments. In particular, complex flow and acoustic interactions with passive and active noise control means can be clearly revealed with this technique.

Acknowledgments

The authors acknowledge use of computational resources from the Yellowstone cluster awarded by the National Science Foundation to CTR. The authors appreciate valuable discussions with Prof. Kai Schneider about the wavelet technique during the CTR program.

REFERENCES

- AMIET, R.K. 1976 Noise due to turbulent flow past a trailing edge. *J. Sound Vib.* **47**, 387–393.
- AZZALINI, A., FARGE, M. & SCHNEIDER, K. 2005 Nonlinear wavelet thresholding: a recursive method to determine the optimal denoising threshold. *Appl. Comput. Harmon.* **18**, 177–185.
- BODLING, A. & SHARMA, A. 2019 Numerical investigation of noise reduction mechanisms in a bio-inspired airfoil. *J. Sound Vib.* **453**, 314–327.
- BROOKS, T.F., POPE, D.S. & MARCOLINI, M.A. 1989 Airfoil self-noise and prediction. *Ref. Rpt. 1218, NASA*.
- BROUZET, D. 2020 Investigation of direct combustion noise in turbulent premixed jet flames using direct numerical simulations. PhD Dissertation, *University of Melbourne*.
- DONOHO, D.L. & JOHNSTONE, J.M. 1994 Ideal spatial adaptation by wavelet shrinkage. *Biometrika* **81**, 425–455.
- FARGE, M. 1992 Wavelet transforms and their application to turbulence. *Annu. Rev. Fluid Mech.* **24**, 395–457.
- GEUZAINÉ, C. & REMACLE, J.F. 2009 Gmsh: a three-dimensional finite element mesh generator with built-in pre- and post-processing facilities. *Int. J. Numer. Methods. Eng.* **79**, 1309–1331.
- GREENWOOD, E., BRENTNER, K.S., RAU, R.F. & TED GAN, Z.F. 2022 Challenges and opportunities for low noise electric aircraft. *Int. J. Aeroacoust.* **22**, 315–381.
- KANG, D. & LEE, S. 2022 Application of wavelet analysis to trailing-edge noise. *AIAA Paper 2022-2891*.
- KANG, D. & LEE, S. 2022 Assessment of wavelet-based separation algorithms on turbulent boundary layer trailing-edge noise prediction. *International Conference on Computational Fluid Dynamics 11*.
- LEE, S. 2018 Empirical wall-pressure spectral modeling for zero and adverse pressure gradient flows. *AIAA J.* **56**, 1818–1829.
- LEE, S. & SHUM, J. 2019 Prediction of airfoil trailing edge noise using empirical wall pressure spectrum models. *AIAA J.* **57**, 888–897.
- LEE, S., AYTON, L., BERTAGNOLIO, F., MOREAU, S., CHONG, T.P. & JOSEPH, P. 2021 Turbulent boundary layer trailing-edge noise: theory, computation, experiment, and application. *Prog. Aerosp. Sci.* **126**, 100737.
- LI, S. & LEE, S. 2020 Prediction of rotorcraft broadband trailing-edge noise and parameter sensitivity study. *J. Am. Helicopter Soc.* **65**, 042006.
- LI, S. & LEE, S. 2021 Prediction of urban air mobility multi-rotor VTOL broadband noise using UCD-QuietFly. *J. Am. Helicopter Soc.* **66**, 032004.
- LI, S. & LEE, S. 2022 Acoustic analysis and sound quality assessment of a quiet helicopter for air taxi operations. *J. Am. Helicopter Soc.* **67**, 032001.
- MANCINELLI, M., PAGLIAROLI, T., DI MARCO, A., CAMUSSI, R. & CASTELAIN, T. 2017 Wavelet decomposition of hydrodynamic and acoustic pressures in the near field of the jet. *J. Fluid Mech.* **813**, 716–749.
- NGUYEN VAN YEN, R., FARGE, M. & SCHNEIDER, K. 2012 Scale-wise coherent vorticity extraction for conditional statistical modeling of homogeneous isotropic two-dimensional turbulence. *Physica D* **241**, 186–201.

- SCHNEIDER, K. & VASILYEV, O.V. 2010 Wavelet methods in computational fluid dynamics. *Annu. Rev. Fluid Mech.* **42**, 473–503.
- WELLER, H.G., TABOR, G., JASAK, H. & FUREBY, C. 1998 A tensorial approach to computational continuum mechanics using object-oriented techniques. *Comput. Phys.* **12**, 620–631.
- WOLF, W.R. & LELE, S.K. 2012 Trailing-edge noise predictions using compressible large-eddy simulation and acoustic analogy. *AIAA J.* **50**, 2423–2434.